Title
Coupled forward-adjoint monte carlo simulations of radiative transport for the study of optical probe design in heterogeneous tissues

Journal
SIAM Journal on Applied Mathematics, 68(1)

ISSN
0036-1399

Authors
Hayakawa, Carole K.
Spanier, Jerome
Venugopalan, Vasan

Publication Date
2007

Peer reviewed

SIAM J. APPL. MATH.
Vol. 68, No. 1, pp. 253–270

COUPLED FORWARD-ADJOINT MONTE CARLO SIMULATIONS OF RADIATIVE TRANSPORT FOR THE STUDY OF OPTICAL PROBE DESIGN IN HETEROGENEOUS TISSUES*

CAROLE K. HAYAKAWA†, JEROME SPANIER‡, AND VASAN VENUGOPALAN†

Abstract. We introduce a novel Monte Carlo method for the analysis of optical probe design that couples a forward and an adjoint simulation to produce spatial-angular maps of the detected light field within the tissue under investigation. Our technique utilizes a generalized reciprocity theory for radiative transport and is often more efficient than using either forward or adjoint simulations alone. For a given probe configuration, the technique produces rigorous, transport-based estimates of the joint probability that photons will both visit any specified target subvolume and be detected. This approach enables the entire tissue region to be subdivided into a collection of target subvolumes to provide a phase-space map of joint probabilities. Such maps are generated efficiently using only one forward and one adjoint simulation for a given probe configuration. These maps are used to identify those probe configurations that best interrogate targeted subvolumes. Inverse solutions in a layered tissue model serve to illustrate and reinforce our analysis.

Key words. Monte Carlo methods, radiative transfer, inverse problems, biological applications

AMS subject classifications. 65C05, 85A25, 34A55, 78A70, 92C55

DOI. 10.1137/060653111

1. Introduction.

The use of light for noninvasive, in vivo determination of optical and physiological properties of tissue volumes is established for a host of applications in biomedical optics. In some cases, other imaging modalities, such as x-ray, ultrasound, or MRI, are used in conjunction with optical techniques to identify heterogeneous tissue regions that require further analysis. Knowledge of this structural information can provide information critical to the design of optical probes to target these regions effectively or to provide information regarding both the target region and its surroundings.

With these goals in mind, much effort has been expended in improving the design of optical probes. For example, there have been attempts to enhance the light delivered to specific tissue regions by varying source and detector characteristics such as orientation, size, angle of emission (for sources), angle of acceptance (for detectors), source-detector (s-d) separation, and/or distance between the target volume and the source/detector [6, 8, 14, 16, 21, 22, 31]. These optical probes are configured in an attempt to enhance the light that is both delivered to the targeted volume and subsequently detected at the tissue surface. Clearly, detailed knowledge of the spatial-angular distribution of the detected light field for a given probe configuration would serve to assess the effectiveness of these approaches and provide a basis to compare competing probe designs.

*Received by the editors February 23, 2006; accepted for publication (in revised form) July 3, 2007; published electronically November 7, 2007. This research was supported by National Institutes of Health grants P41-RR-00192 (Laser Microbeam and Medical Program) and R01-EB-00345.
http://www.siam.org/journals/siap/68-1/65311.html
†Laser Microbeam and Medical Program, Beckman Laser Institute, University of California—Irvine, Irvine, CA 92612-3010, and Department of Chemical Engineering and Materials Science, University of California—Irvine, Irvine, CA 92697-2575 (hayakawa@uci.edu).
‡Laser Microbeam and Medical Program, Beckman Laser Institute, University of California—Irvine, Irvine, CA 92612-3010.

Previous studies of radiative transfer in tissue from source to detector have been based mainly on the diffusion approximation to the radiative transport equation [3, 7, 15, 17]. However, the validity of diffusion-based models is compromised when (a) s-d separations are small or (b) the tissue absorption is comparable to or greater than scattering. While analytic [27] and specific Monte Carlo [2] approaches have been investigated, it is unclear how these methodologies would extend to heterogeneous media. Moreover, conventional Monte Carlo simulations provide results with large uncertainties in the detected signals due to the small detector sizes often used in optical probes.

To address this problem in the context of radiative transport, we have developed a novel Monte Carlo method that produces phase-space maps to provide quantitative measures of the ability for a given probe configuration to detect light delivered to specific regions within the tissue. This general approach can be applied to complex, heterogeneous media. The method makes use of coupled forward-adjoint simulations to estimate the joint probability of both visitation of a target region and subsequent detection at the tissue surface. Bayes's theorem [12] is used to decompose this joint probability into the product of an absolute and a conditional probability. These two probabilities are then estimated using separate and efficient simulations. In cases for which the targeted volume is large compared to both source and detector volumes, the gains in efficiency over the use of either a forward or an adjoint simulation alone can be substantial.

In this paper, we describe the foundations of our method as well as its operational details. We then apply the method to investigate how a layered epithelial tissue is interrogated by optical probe designs in which we allow variation in s-d separation. Forward and adjoint simulations are generated for various probe configurations. The simulation results are used to produce maps that provide both qualitative and quantitative information regarding the phase-space distribution of the detected light. This information provides a basis for the comparison of prospective probe designs to determine the merits of each. Accurate recovery of optical properties from heterogeneous tissues via inverse solutions serves to confirm the comparative analysis of candidate probe designs as evaluated by the coupled forward-adjoint Monte Carlo simulations.

2. Method. To determine the probability of detecting light that has visited a targeted volume, one could utilize a conventional Monte Carlo simulation in which one follows photon trajectories from the source to a target volume and then tallies the final photon weight for those photons that are subsequently detected. Alternatively, one could use an adjoint Monte Carlo simulation, in which one follows backward-propagating photons from the detector to the target volume, and then to the source. However, when the source and detector are each small relative to the target volume, sole use of a forward or adjoint simulation engenders low signal-to-noise ratios (SNRs). Such a situation is exceedingly common in biomedical optics.

Our approach is to break the problem into two components and determine separately (a) the probability of source to target trajectories, $P(V)$ ("target visitation"), and (b) the probability of detection conditioned by target visitation, $P(D|V)$ ("detection given target visitation"). The combination of these two probabilities using Bayes's theorem provides the rigorous joint transport probability of "target visitation and detection":

$$P(V \cap D) = P(V) \cdot P(D|V). \tag{2.1}$$

We use a conventional Monte Carlo simulation to determine $P(V)$. However, for

$P(D|V)$, we utilize an adjoint simulation to combat the inherently low SNR in its estimation in the reverse direction. This is done by modifying a generalized reciprocity principle [5, 19, 25, 29] to convert $P(D|V)$ to a coupled forward-adjoint computation at the surface of the target volume.

In the next section, we describe our application of coupled forward-adjoint Monte Carlo methods for the determination of $P(V \cap D)$. This includes a review of classical reciprocity theory and basic equations. We then describe generalized reciprocity, for which classical reciprocity is a special case. Finally, we develop our extension of generalized reciprocity theory to arrive at an estimate of $P(V \cap D)$. This will set the stage for the application of this methodology to problems in biomedical optics.

3. Coupled forward-adjoint Monte Carlo methods. A series of publications [5, 19, 20, 25, 24, 30, 29] has developed and described the "midway" forward-adjoint coupling method to increase the efficiency of estimating detector responses in radiative transport problems. The idea is to simulate both forward and adjoint Monte Carlo transport and combine the tallies from each at an intermediate surface to estimate the total system response. The midway method is made rigorous by appealing to a generalized reciprocity theory for transport equations [19, 20, 29, 30]. The midway method has been shown to be particularly efficient in problems that involve deep penetration and/or complex streaming pathways taken by the radiation as it moves from source(s) to detector(s) [19, 20, 24, 25].

We modify the midway method in order to apply it to the estimation of the conditional probability $P(D|V)$. Photons are launched at a physical source and are propagated until they exit the phase space. At each interaction within the tissue, the photon weight is reduced according to its survival probability, a technique sometimes referred to as "absorption weighting" [23]. Only photon trajectories that have intersected the target volume $\mathbb{V}$ contribute to the estimate of $P(V)$. These "visiting" photons generate an induced source internal to $\mathbb{V}$ that produces a surface source on $\partial\mathbb{V}$. This surface source is then paired with the adjoint flux on $\partial\mathbb{V}$ in a bilinear integration that produces an estimate of $P(D|V)$. The product of the two probabilities $P(V)$ and $P(D|V)$ then provides the probability that photons will both visit and subsequently be detected from subvolumes within the phase space. We use this product to provide quantitative information to assess the characteristics of potential probe designs.

3.1. Classical reciprocity. We begin with the integro-differential form of the radiative transport equation (RTE) assumed to hold in the interior of a closed, bounded subset $\mathbb{D}$ of $\mathbb{R}^3$:

$$\nabla \cdot \mathbf{\Omega}\, \Phi(\mathbf{r}, \mathbf{\Omega}) + \mu_t(\mathbf{r})\Phi(\mathbf{r}, \mathbf{\Omega}) = \mu_s(\mathbf{r}) \int_{4\pi} f(\mathbf{\Omega}' \to \mathbf{\Omega})\Phi(\mathbf{r}, \mathbf{\Omega}')\, d\mathbf{\Omega}' + Q(\mathbf{r}, \mathbf{\Omega}), \tag{3.1}$$

where $\Phi(\mathbf{r}, \mathbf{\Omega})$ is the photon flux, $\mu_t(\mathbf{r}) = \mu_s(\mathbf{r}) + \mu_a(\mathbf{r})$ is the total attenuation coefficient, $\mu_s(\mathbf{r})$ is the scattering coefficient, $\mu_a(\mathbf{r})$ is the absorption coefficient, $f(\mathbf{\Omega}' \to \mathbf{\Omega})$ is the single scattering phase function, and $Q(\mathbf{r}, \mathbf{\Omega})$ is an internal (volumetric) source function, with $\mathbf{r} = (x, y, z)$ and $\mathbf{\Omega} = (\sin\theta\cos\phi, \sin\theta\sin\phi, \cos\theta)$ representing position and unit direction vectors, respectively. A unique solution $\Phi(\mathbf{r}, \mathbf{\Omega})$ is assured for all $\mathbf{r} \in \mathbb{D}$, $\mathbf{\Omega} \in S^2$ by specifying the photon flux $\Phi_{\text{inc}}(\mathbf{r}, \mathbf{\Omega})$ incident on $\partial\mathbb{D}$ from outside the tissue. We introduce an abbreviated form of (3.1):

$$\nabla \cdot \mathbf{\Omega}\Phi + \mathcal{B}\Phi = Q, \tag{3.2}$$

where $\mathcal{B}$ denotes the transport operator less the divergence term.

A typical optical probe is an instrument that both introduces light at the tissue boundary and collects light reemitted from the boundary using or more detectors positioned at fixed distances from the source. Assuming that there are no other (external) sources of light, the unique solution Φ of this RTE can be written as a superposition of the photon fluxes produced by the internal source Q and the boundary source Q_s defined by

$$Q_s(\mathbf{r}_s, \mathbf{\Omega}) = -\mathbf{\Omega} \cdot \mathbf{n}_s \Phi_{\text{inc}}(\mathbf{r}_s, \mathbf{\Omega}) \quad \text{for } \mathbf{r}_s \in \partial\mathbb{D},\ \mathbf{\Omega} \cdot \mathbf{n}_s < 0, \tag{3.3}$$

where $\mathbf{n}_s$ is the outward-pointing unit normal at r_s:

$$\begin{aligned}\Phi(\mathbf{r}, \mathbf{\Omega}) = &\int_{\mathbb{D}\times S^2} G[(\mathbf{r}_0, \mathbf{\Omega}_0) \to (\mathbf{r}, \mathbf{\Omega})] Q(\mathbf{r}_0, \mathbf{\Omega}_0)\, d\mathbf{r}_0\, d\mathbf{\Omega}_0 \\ &+ \int_{\partial\mathbb{D}\times S^2} G_s[(\mathbf{r}_0, \mathbf{\Omega}_0) \to (\mathbf{r}, \mathbf{\Omega})] \Phi_{\text{inc}}(\mathbf{r}_s, \mathbf{\Omega}_s)\, d\mathbf{r}_0\, d\mathbf{\Omega}_0,\end{aligned} \tag{3.4}$$

where G is the volume Green's function and G_s is the surface Green's function for the problem. An alternate, equivalent representation that uses only the volume Green's function is

$$\Phi(r, \Omega) = \int_{\mathbb{D}\times S^2} G[(\mathbf{r}_0, \mathbf{\Omega}_0) \to (\mathbf{r}, \mathbf{\Omega})] Q(\mathbf{r}_0, \mathbf{\Omega}_0)\, d\mathbf{r}_0\, d\mathbf{\Omega}_0, \tag{3.5}$$

where the second term in (3.4) is replaced by the boundary condition

$$\Phi(\mathbf{r}_s, \mathbf{\Omega}_s) = Q_s(\mathbf{r}_s, \mathbf{\Omega}_s) \tag{3.6}$$

and Q_s is defined as in (3.3) [4]. The relationship (3.3) and the equivalence between the representations (3.4) and (3.5) together with (3.6) will be utilized in section 3.3.

The response of either a virtual or a physical detector can then be described in terms of a linear functional of Φ:

$$I = \int_{\mathbb{D}\times S^2} Q^* \Phi\, d\mathbf{r}\, d\mathbf{\Omega}, \tag{3.7}$$

where Q^* characterizes the detector position, size, and acceptance angle. Both the source function Q and detector function Q^* may be described mathematically using characteristic functions associated with the source and detector. For example, if the tissue $\mathbb{D}$ is assumed to occupy the half space characterized in rectangular coordinates by $z > 0$, and a fiber-optic laser source of radius q and unit strength is normally incident at $(0, 0, 0)$, we have

$$Q_s(x_s, y_s, 0, \mathbf{\Omega}) = \begin{cases} 1, & x_s^2 + y_s^2 \le q^2 \quad \text{and} \\ & -1 \le \mathbf{n}_{\mathbb{D}} \cdot \mathbf{\Omega} < -\cos\theta_Q, \\ 0 & \text{otherwise,} \end{cases} \tag{3.8}$$

where $\mathbf{n}_{\mathbb{D}}$ denotes the outward-pointing unit normal at the bounding surface $z = 0$ and the source is confined to an emission angle θ_Q. A similar description characterizes a typical fiber-optic detector placed elsewhere on the tissue surface $z = 0$, except that it collects light that scatters *into* the half space $z < 0$ at location $(X_{Q^*}, Y_{Q^*}, 0)$ within the detector radius q^* and acceptance angle θ_{Q^*}. Specifically,

$$Q_s^*(x_s, y_s, 0, \mathbf{\Omega}) = \begin{cases} 1, & (x_s - X_{Q^*})^2 + (y_s - Y_{Q^*})^2 \le (q^*)^2 \quad \text{and} \\ & 1 \ge \mathbf{n}_{\mathbb{D}} \cdot \mathbf{\Omega} > \cos\theta_{Q^*}, \\ 0 & \text{otherwise.} \end{cases} \tag{3.9}$$

It is well known that classical reciprocity theory also permits the detector response I to be expressed as a linear functional of the solution to the RTE that is adjoint to (3.1) [23]:

(3.10)
$$-\nabla \cdot \mathbf{\Omega}\, \Phi^*(\mathbf{r}, \mathbf{\Omega}) + \mu_t(\mathbf{r})\Phi^*(\mathbf{r}, \mathbf{\Omega}) = \mu_s(\mathbf{r}) \int_{4\pi} f(\mathbf{\Omega} \to \mathbf{\Omega}')\Phi^*(\mathbf{r}, \mathbf{\Omega}')\, d\mathbf{\Omega}' + Q^*(\mathbf{r}, \mathbf{\Omega})$$

and

$$I = \int_{\mathbb{D}\times S^2} Q\Phi^*\, d\mathbf{r}\, d\mathbf{\Omega}. \tag{3.11}$$

Upon comparing the detector response representations (3.7) and (3.11), we notice that the roles of the source function Q and detector function Q^* are interchanged in this statement of reciprocity, so that Q acts as a "detector" function for the adjoint formulation and Q^* plays the role of a "source" function for the adjoint equation.

Using operator notation, (3.10) can be written as

$$-\nabla \cdot \mathbf{\Omega}\Phi^* + \mathcal{B}^*\Phi^* = Q^*, \tag{3.12}$$

where $\mathcal{B}^*$ is the operator adjoint to $\mathcal{B}$. For (3.11) to be valid, it is also understood that the boundary condition satisfied by Φ^* on $\partial\mathbb{D}$ is dual to that specified for Φ. For example, in our application $\partial\mathbb{D}$ is the surface of the tissue that is composed of the source region A_Q, the detector region A_{Q^*}, and the complement of these two regions $\partial\mathbb{D}\backslash(A_Q \cup A_{Q^*})$. Here we assume for simplicity that both the source emission angle and the detector acceptance angle are fully open; i.e., $\cos\theta_Q = \cos\theta_{Q^*} = 0$. For this case, the boundary condition at $z = 0$ satisfied by Φ is

$$\Phi(x_s, y_s, 0, \mathbf{\Omega}) = Q_s(x_s, y_s, 0, \mathbf{\Omega}) \quad \text{for } (x_s, y_s) \in A_Q, \tag{3.13}$$

where the right-hand side is defined by (3.8) with $\cos\theta_Q = 0$. The dual boundary condition for Φ^* becomes

$$\Phi^*(x_s, y_s, 0, \mathbf{\Omega}) = Q_s^*(x_s, y_s, 0, \mathbf{\Omega}) \quad \text{for } (x_s, y_s) \in A_{Q^*}, \tag{3.14}$$

where the right-hand side is defined by (3.9) with $\cos\theta_{Q^*} = 0$. From (3.13) and (3.14) we have $\Phi\Phi^* = 0$ on $\partial\mathbb{D}$ establishing that the boundary conditions are dual to each other. Note that (3.13) and (3.14) are incomplete statements of the boundary conditions for $\mathbf{r} \in \partial\mathbb{D}\backslash(A_Q \cup A_{Q^*})$, as they do not include the full range of $\mathbf{\Omega}$. The missing conditions for our case accommodates a tissue-air refractive index mismatch using the Fresnel relations for unpolarized light [28]. This results in a mixed boundary condition comprised of a linear combination of reflecting and nonreentrant conditions, each component of which leads to duality as shown by Aronson [1].

The duality of the governing equations and boundary conditions enables a detector response to be computed *either* in the context of forward Monte Carlo sampling *or* adjoint Monte Carlo sampling via this "classical" reciprocity for the RTE. Usually one of these formulations will lead to a more efficient simulation than the other. However, many problems in biomedical optics utilize *both* small sources *and* small detectors, making *neither* formulation efficient.

However, we can improve the efficiency of classical reciprocity by utilizing a midway surface between source and detector. The midway method combines forward and adjoint sampling that characterizes those photons that have migrated from source to detector through a separating midway surface. Application of generalized reciprocity to the estimation of $P(D|V)$ using this midway method will then lead us to our final evaluation of $P(V \cap D)$. In section 3.2 we explain generalized reciprocity and the midway method. In section 3.3 we extend these ideas to compute the joint probability of visitation and detection $P(V \cap D)$.

3.2. Generalized reciprocity. Let us first consider $\mathbb{V}_M$ to be an arbitrary closed, bounded subset of $\mathbb{D}$ and $\partial\mathbb{V}_M$ its surface. Multiplying (3.2) by Φ^* and (3.12) by Φ, subtracting the latter product from the former, and integrating the difference over all locations and directions within V_M, we get

$$\int_{\mathbb{V}_M \times S^2} \nabla \cdot \mathbf{\Omega} \Phi \Phi^* \, d\mathbf{r} \, d\mathbf{\Omega} = \int_{\mathbb{V}_M \times S^2} [Q\Phi^* - Q^*\Phi] \, d\mathbf{r} \, d\mathbf{\Omega}. \tag{3.15}$$

Use of Green's theorem to replace the volume integral on the left-hand side of (3.15) by a surface integral leads to

$$\int_{\partial\mathbb{V}_M \times S^2} \mathbf{n}_M \cdot \mathbf{\Omega} \Phi \Phi^* \, d\mathbf{r} \, d\mathbf{\Omega} = \int_{\mathbb{V}_M \times S^2} [Q\Phi^* - Q^*\Phi] \, d\mathbf{r} \, d\mathbf{\Omega}, \tag{3.16}$$

where $\mathbf{n}_M$ is the outward-pointing unit vector normal to $\partial\mathbb{V}_M$. Equation (3.16) is often referred to as the global reciprocity theorem [30]. Note that if $\mathbb{V}_M = \mathbb{D}$ and the boundary conditions at the air-tissue interface cause the integral on the left-hand side to vanish (as is the case in our problem), we then arrive at the "classical" statement of reciprocity:

$$\int_{\mathbb{V}_M \times S^2} [Q\Phi^* - Q^*\Phi] \, d\mathbf{r} \, d\mathbf{\Omega} = 0. \tag{3.17}$$

While (3.16) is valid generally, it becomes particularly useful when $\mathbb{V}_M$ encloses *either* the source *or* the detector region. The surface of $\mathbb{V}_M$, $\partial\mathbb{V}_M$, can then be identified as a "midway" surface between source and detector. In this case, every photon that is detected from the source *must* intersect the midway surface.

The function $\Phi\Phi^*$ that occurs in (3.16) has been called a "contributon" response function [5, 19, 20, 24, 25, 29, 30] and used to define a unit of information that characterizes transport from source to detector. The integral of this function appearing on the left-hand side of (3.16) plays a similar role here. It captures the flow of information across the boundary of the midway volume $\mathbb{V}_M$.

If $\mathbb{V}_M$ encloses the source region as shown in Figure 3.1(a) and $Q^* = 0$ in $\mathbb{V}_M$, the left-hand side of (3.16) is positive and equals $\int_{\mathbb{V}_M \times S^2} Q\Phi^*$, which is the adjoint representation of the detector response. If $\mathbb{V}_M$ encloses the detector region, and $Q = 0$ in $\mathbb{V}_M$, the left-hand side of (3.16) is negative and equals $-\int_{\mathbb{V}_M \times S^2} Q^*\Phi$, which is the forward representation of the detector response. Reversing the sense of $\mathbf{n}_M$ by replacing the outward-pointing unit normal with the inward-pointing unit normal changes the sign in the surface integral on the left-hand side of (3.16) and also reverses the sense of enclosure. That is, if $\mathbb{V}_M$ is treated as an enclosure for the source, then $\mathbf{n}_M$ points outward. However, if the complement of $\mathbb{V}_M$ in $\mathbb{D}$, $\mathbb{D}\backslash\mathbb{V}_M$, is treated as an enclosure for the detector, then $\mathbf{n}_M$ points inward.

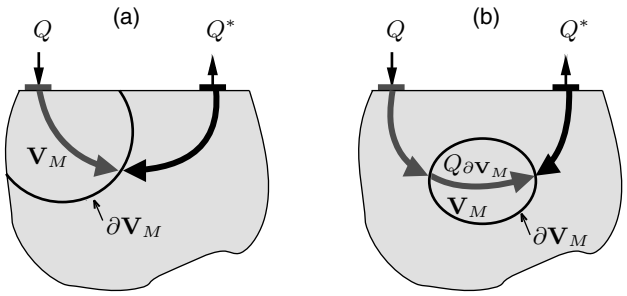

FIG. 3.1. *Geometry of* (a) *generalized reciprocity with the midway surface* $\partial\mathbf{V}_M$ *enclosing the physical source, and* (b) *an extension to generalized reciprocity with an induced boundary source* $Q_{\partial\mathbf{V}_M}$ *out of* $\mathbf{V}_M$ *used to compute conditional probabilities.*

In many situations, this midway surface method proves to be more efficient than using either the forward or adjoint simulation alone [19, 20]. The gains in efficiency will largely be the consequence of the relatively larger "size" of $\mathbb{V}_M$ compared with either the size of the source region, where $Q \neq 0$, or of the detector region, where $Q^* \neq 0$. Here "size" is to be interpreted in a probability sense as opposed to a strict physical size. More precisely, the relevant condition is that the probability of reaching $\mathbb{V}$ from either the source or detector should be larger than the corresponding probabilities in the reverse directions.

3.3. Probability of visitation and detection. The probe design problem requires an understanding of more than the *total* system response at the detector from the original optical source. It requires, in addition, knowledge of the detector response due *only* to those photons that have visited a targeted tissue region $\mathbb{V}$. For our application, $\mathbb{V}$ is a region that encloses *neither* the source *nor* the detector. Thus, to make use of generalized reciprocity, we treat $\mathbb{V}$ as a region that generates a secondary or "virtual" source, induced by the original physical source. This construct allows us to decompose the problem into two subproblems. The first problem deals only with the estimation of $P(V)$ and is handled using conventional Monte Carlo simulation. The second problem handles the estimation of $P(D|V)$ and will be accomplished by a suitable application of the generalized reciprocity relation (3.16).

Accordingly, the midway volume $\mathbb{V}_M$ can be considered as an arbitrary volume enclosing neither source nor detector with surface $\partial\mathbb{V}_M$. A possible geometry is shown in Figure 3.1(b). This arbitrary volume $\mathbb{V}_M$ is one at whose boundary, $\partial\mathbb{V}_M$, information will be collected from both forward and adjoint photons for the estimation of $P(V)$ and $P(D|V)$, respectively. We estimate the first factor of (2.1), $P(V)$, by launching photons from the original source Q characterized in (3.8) and, for those photons that enter $\mathbb{V}_M$, tally the entering weight of each photon. These photons produce estimates of $P(V)$ and generate samples drawn from an induced source $Q_{\partial\mathbb{V}_M}$ impinging on $\partial\mathbb{V}_M$ from *inside* $\mathbb{V}_M$. The boundary surface $\partial\mathbb{V}_M$ then defines the surface for the midway method applied to the problem of estimating the conditional probability, $P(V|D)$.

The details of the required computation deserve elaboration. Denote $\Phi(\mathbf{r}, \mathbf{\Omega})$ as the solution of the boundary-value problem of (3.1) with source described as in (3.8), and let $\Phi_{\mathbb{V}_M}(\mathbf{r}, \mathbf{\Omega})$ denote the restriction of $\Phi(\mathbf{r}, \mathbf{\Omega})$ to $\mathbf{r} \in \mathbb{V}_M$. The photon flux $\Phi_{\partial\mathbb{V}_M}(\mathbf{r}, \mathbf{\Omega})$ for $\mathbf{r} \in \partial\mathbb{V}_M$, $\mathbf{\Omega} \cdot \mathbf{n}_{\partial\mathbb{V}} < 0$, where $\mathbf{n}_{\partial\mathbb{V}}$ = unit normal out of $\mathbb{V}_M$ (*into* $\mathbb{D}\backslash\mathbb{V}$) then generates a boundary source $Q_{\partial\mathbb{V}_M}(\mathbf{r}_s, \mathbf{\Omega}_s) = -\Omega_s \cdot \mathbf{n}_{\partial\mathbb{V}_M} \Phi_{\partial\mathbb{V}_M}(\mathbf{r}_s, \mathbf{\Omega}_s)$ on

$\partial\mathbb{V}_M$. If we merely replace the source function Q by the source function $Q_{\partial\mathbb{V}}(\mathbf{r},\mathbf{\Omega})$ and repeat the derivation that led to (3.16), we obtain

$$\int_{\partial\mathbb{V}_M\times S^2}\mathbf{n}_{\partial\mathbb{V}_M}\cdot\mathbf{\Omega}\Phi_{\mathbb{V}_M}\Phi^*\,d\mathbf{r}\,d\mathbf{\Omega}=\int_{\mathbb{V}_M\times S^2}[Q_{\partial\mathbb{V}_M}\Phi^*-Q^*\Phi_{\mathbb{V}_M}]\,d\mathbf{r}\,d\mathbf{\Omega}. \tag{3.18}$$

We replace $Q^*(\mathbf{r},\mathbf{\Omega})$ by $Q^*(\mathbf{r},-\mathbf{\Omega})$ to generate an adjoint flux, $\Phi^*(\mathbf{r},-\mathbf{\Omega})$, *inside* the tissue. This, of course, reverses the direction in the arguments of Q^* and Φ^* in (3.18), which then reads

$$\begin{aligned}\int_{\partial\mathbb{V}_M\times S^2}&\mathbf{n}_{\partial\mathbb{V}_M}\cdot\mathbf{\Omega}\Phi_{\mathbb{V}_M}(\mathbf{r},\mathbf{\Omega})\Phi^*(\mathbf{r},-\mathbf{\Omega})\,d\mathbf{r}\,d\mathbf{\Omega}\\&=\int_{\mathbb{V}_M\times S^2}[Q_{\partial\mathbb{V}_M}(\mathbf{r},\mathbf{\Omega})\Phi^*(\mathbf{r},-\mathbf{\Omega})-Q^*(\mathbf{r},-\mathbf{\Omega})\Phi_{\mathbb{V}_M}(\mathbf{r},\mathbf{\Omega})]\,d\mathbf{r}\,d\mathbf{\Omega}\\&=\int_{\mathbb{V}_M\times S^2}Q_{\partial\mathbb{V}_M}(\mathbf{r},\mathbf{\Omega})\Phi^*(\mathbf{r},-\mathbf{\Omega})\,d\mathbf{r}\,d\mathbf{\Omega}\end{aligned} \tag{3.19}$$

since $Q^*=0$ inside $\mathbb{V}_M$. Estimation of (3.19) is performed using an adjoint simulation and provides the detected response due to the induced source $Q_{\partial\mathbb{V}_M}$, or $P(D|V)$.

The forward simulation of photons exiting an arbitrary target volume $\mathbb{V}_M$ is used to determine $P(V)$ and is matched with the adjoint simulation estimate of $P(D|V)$ at $\partial\mathbb{V}_M$. The joint probability of visitation and detection $P(V\cap D)$ (see (2.1)) is formed by the product of these two factors. The resulting probability characterizes a three body system involving radiative transport from (a) the original source Q to (b) the target volume $\mathbb{V}_M$ and finally to (c) the detector. In what follows, we shall refer to joint probability of visitation and detection of the target volume, $P(V\cap D)$, as *interrogation* of the target volume.

4. Implementation. Monte Carlo simulations of both the forward RTE equation (3.1) and the adjoint RTE (3.10) are quite conventional [10, 26]. Photon and adjoint photon biographies are generated by alternately sampling from exponential distributions representing intercollision distances and angular deflections sampled from the Henyey–Greenstein phase function [11, 28]. The resulting random walks are followed until they escape the tissue phase space.

We utilize our coupled forward-adjoint methodology to create quantitative maps of the entire tissue that illustrate how the light interrogates various regions in the tissue. We shall refer to these maps as "interrogation maps." To create such maps, the tissue is subdivided into a finite number of voxels, each treated as a target volume $\mathbb{V}$. The matching of photon trajectories between the forward simulation and the adjoint simulation occurs at the boundary of each voxel. The integration shown on the left-hand side of (3.19) requires the pairing of estimates of the photon current $J=\mathbf{n}_{\partial\mathbb{V}_M}\cdot\mathbf{\Omega}\tilde{\Phi}$ from the forward simulation with the estimation of the photon flux Φ^* from the adjoint simulation. Upon exiting a voxel $\mathbb{V}$, both the location and orientation of the photon's track are assigned to one of $N_{\partial\mathbb{V}}\cdot N_\mu\cdot N_\phi$ spatial-angular bins:

$$\Delta_{ijk}:\begin{cases}\mathbf{r}\in\partial\mathbb{V}_i, & i=1,\dots,N_{\partial\mathbb{V}},\\ \frac{2(j-1)}{N_\mu}<(\mu+1)\le\frac{2j}{N_\mu}, & j=1,\dots,N_\mu,\\ \frac{2\pi(k-1)}{N_\phi}<\phi\le\frac{2\pi k}{N_\phi}, & k=1,\dots,N_\phi.\end{cases} \tag{4.1}$$

Each solid angle bin is determined by $\mu=\cos\theta$ and ϕ, where θ is the polar angle and ϕ is the azimuthal angle. The north pole for the directional system is taken to be the

outward-pointing normal on each voxel side. Trajectories in the forward simulation that *exit* bin Δ_{ijk} are matched with trajectories in the adjoint simulation that *enter* the same angular bin. We determine $P(V \cap D)$ for each voxel $\mathbb{V}$ by summing the product of the tallies of the forward and adjoint photons in the matched spatial-angular pairs over all bins:

$$P(V \cap D) = \sum_{i}^{N_{\partial \mathbb{V}}} \sum_{j}^{N_{\mu}} \sum_{k}^{N_{\phi}} J_{ijk} \Phi^{*}_{ijk} \Delta \partial \mathbb{V}_i \Delta \mu_j \Delta \phi_k. \tag{4.2}$$

In (4.2), J_{ijk} is estimated by tallying the photon weight w_{ijk} per unit area and solid angle upon exiting the voxel surface

$$J_{ijk} = \frac{1}{N_F} \sum_{n=1}^{N_F} \frac{w^{(n)}_{ijk}}{\Delta \partial \mathbb{V}_i \Delta \mu_j \Delta \phi_k}, \tag{4.3}$$

where N_F is the number of photons launched in the forward simulation. The adjoint simulation converts the adjoint current to an adjoint flux via the relation

$$\Phi^{*}_{ijk} = \frac{J^{*}_{ijk}}{\mu_j}, \tag{4.4}$$

where μ_j is the polar cosine of the entering photon. The weight w^{*}_{ijk} of each adjoint photon entering the voxel surface is then used in the estimate of the adjoint current

$$J^{*}_{ijk} = \frac{1}{N_A} \sum_{n=1}^{N_A} \frac{w^{*(n)}_{ijk}}{\Delta \partial \mathbb{V}_i \Delta \mu_j \Delta \phi_k}, \tag{4.5}$$

where N_A is the total number of adjoint photons launched. For simplicity, we use uniform spatial and angular bins. In practice, however, we anticipate the need to utilize finer binning closer to the tissue surface and at other locations where the distribution of the light field either is highly anisotropic or possesses large spatial gradients. Sufficiently deep in the tissue, where the flux is expected to be nearly isotropic, a coarse uniform angular grid should suffice.

The variance of our $P(V \cap D)$ estimates is derived as specified in the midway method literature [20]. Specifically, the relative variances of the forward current J_{ijk} and the adjoint flux Φ^{*}_{ijk} are determined by

$$r^2[J_{ijk}] = \frac{\sum_{n=1}^{N_F} \left[w^{(n)}_{ijk} \right]^2}{\left[\sum_{n=1}^{N_F} w^{(n)}_{ijk} \right]^2} - \frac{1}{N_F} \tag{4.6}$$

and

$$r^2[\Phi^{*}_{ijk}] = \frac{1}{\mu_j^2} \left\{ \frac{\sum_{n=1}^{N_A} \left[w^{*(n)}_{ijk} \right]^2}{\left[\sum_{n=1}^{N_A} w^{*(n)}_{ijk} \right]^2} - \frac{1}{N_A} \right\}, \tag{4.7}$$

respectively. Since the quantities of J_{ijk} and Φ^{*}_{ijk} are estimated from forward and adjoint random walks that are sampled independently, a first-order approximation of the relative variance of their product is provided by the sum of their relative variances

$$r^2[J_{ijk} \Phi^{*}_{ijk}] \approx r^2[J_{ijk}] + r^2[\Phi^{*}_{ijk}]. \tag{4.8}$$

The variance of $P(V \cap D)$ is obtained by summing the variances of the products over all bins:

$$\sigma^2[P(V \cap D)] = \sum_i^{N_{\partial \mathbb{V}}} \sum_j^{N_\mu} \sum_k^{N_\phi} r^2[J_{ijk}\Phi^*_{ijk}] J^2_{ijk}\Phi^{*2}_{ijk}. \tag{4.9}$$

Note that (4.9) provides the variance for *each* target volume. For a fixed number of launched (forward and adjoint) photons, an increase in $N_{\partial \mathbb{V}}$, N_μ, and N_ϕ results in an increase in $r^2[J_{ijk}\Phi^*_{ijk}]$ because there are fewer photons per bin and will tend to increase the relative error in the estimate for each bin. While an increase in the number of bins will tend to increase the variance $\sigma^2[P(V \cap D)]$, it will also reduce the discretization error. Optimal choices for $N_{\partial \mathbb{V}}$, N_μ, and N_ϕ vary depending on the precise location of the voxel in the tissue. For the purposes of the results presented in this initial study, we chose uniform spatial and angular binning. An analysis of the optimal binning allocation strategy is beyond the scope of this paper and, in any event, will be highly problem-dependent.

As a means to eliminate the discretization error, we investigated a method proposed by Cramer [5] in which two sets of trajectories are launched at the voxel boundary in *exactly* opposite directions. Each set is then followed until possible detection at the source or detector. However, due to the small size of the fiber-optic source and detector and the large number of target volumes treated in our application, this method was not particularly efficient and was not employed in this study.

Note that while we are summing over all spatial-angular bins in this study, we could easily provide maps containing information for photons entering and exiting at *any* particular set of orientations or locations. This more refined information would enable an evaluation of the impact of angular variations in the light distribution on the conditional system response. Such angular detail will be especially important for voxels in regions in which the light field is highly anisotropic, for example, in the proximity of collimated sources or interfaces of refractive index mismatch.

5. Numerical results. We apply our methodology to a test case depicting epithelial tissue consisting of a thin upper cellular layer ($0 < z < 0.5$ mm) situated above a much thicker structural (stromal) layer ($z > 0.5$ mm). The goal of this study is to assess the effect of probe s-d separation on the interrogation of each layer. We first examine the forward problem; that is, we generate $P(V \cap D)$ spatial-angular maps for normal tissue. We refer to this as our "background" tissue problem. The purpose of these maps is to indicate the effectiveness of a given probe configuration to detect and isolate transformations in each of the layers associated with the formation of precancerous tissue. Simulated data of measured reflectance is then generated that contains information characterizing physiologically relevant changes in one or both layers. This measured data is then used to predict changes in the layered optical properties via an inverse solution that employs a special perturbation and differential Monte Carlo optimization method developed previously [9, 10]. For our particular study in epithelial tissue, we will discuss possible relationships between the information provided by the $P(V \cap D)$ maps and the quality of the inverse solution results.

5.1. Background tissue forward problem. We first consider a homogeneous background tissue with a refractive index $n = 1.4$ and optical properties typical of normal stromal tissue [13] at an optical wavelength of 849 nm: $\mu_a = 0.034$/mm, $\mu_s = 6.11$/mm, $g = 0.9$. Here g is the average cosine of the Henyey–Greenstein single-scattering phase function commonly used for tissue [28]. The probe configurations

considered consist of both source and detector oriented normal to the tissue surface with s-d separations ranging from 1–3 mm. The source and detector have emission and acceptance angles $\theta_Q = \theta_{Q^*} = 15.3°$ relative to their central axis and are 200 μm in radius. To efficiently present the $P(V \cap D)$ results, which constitute a three-dimensional data set, we sum the results of (4.2) along the y-axis and project them onto the x-z plane in 0.1 mm $\times$ 0.1 mm pixels, each of which represents a different target volume $\mathbb{V}$.

Figure 5.1 displays the interrogation $P(V \cap D)$ maps for the background tissue. In this analysis, we compare probe features consisting of s-d separations of 1, 2, and 3 mm. In these plots, the color of every voxel represents the absolute (unscaled) conditional probability of detection (conditioned by visiting the voxel in question). We shall refer to this quantity as the "conditional system response." To enable the visualization of a greater dynamic range in $P(V \cap D)$, the colors are represented on a log scale with a spectrum ranging from large (red (10^{-8})) to small (blue (10^{-11})) probability. A dashed white line at a $z = 0.5$ mm delineates the interface between the two layers of interest. Note that in each of these maps, we display the conditional system response for each voxel. The database so constructed provides the raw material for the analysis of competing probe configurations.

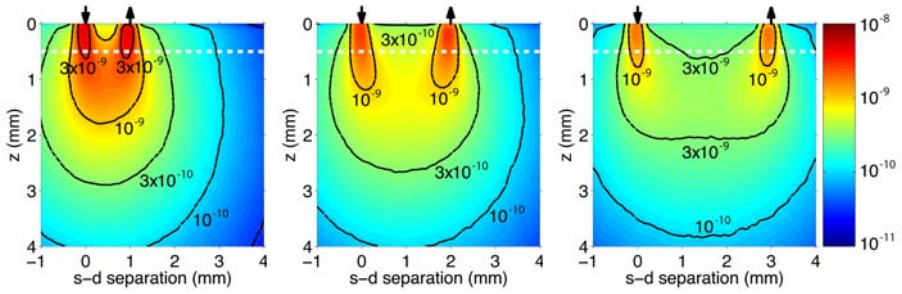

FIG. 5.1. *Interrogation map of the background problem for s-d separations of* 1, 2, *and* 3 *mm (left to right).*

The results of Figure 5.1 can be normalized by the sum of $P(V \cap D)$ over the whole domain $\mathbb{D}$ to produce a true probability density function which we will refer to as an "interrogation density function":

$$p_{V \cap D} = \frac{P(V \cap D)}{\int_{\mathbb{D}} P(V \cap D)}. \tag{5.1}$$

Equation (5.1) provides an appropriate function to assess how a particular region of interest is interrogated. This normalized function allows different probe configurations to be compared on an equivalent basis. For example, we can integrate $p_{V \cap D}$ over the top layer $\mathbb{T}$ or bottom layer $\mathbb{B}$, resulting in $\int_{\mathbb{T}} p_{V \cap D}$ and $\int_{\mathbb{B}} p_{V \cap D}$, respectively. This will provide the relative contribution from each layer to the detected signal in the form of a probability.

Figure 5.2 presents the integration of $p_{V \cap D}$ over the top and bottom layers as a function of s-d separation. These results reveal that roughly four times as much detected signal has interrogated the bottom layer as opposed to the top layer. The bottom layer probabilities increase by 4.5% (from 0.805 to 0.841) as the s-d separation increases from 1 to 3 mm, revealing that the larger s-d separations are more effective in interrogating the bottom layer than the smaller ones. Recall that by "interrogate"

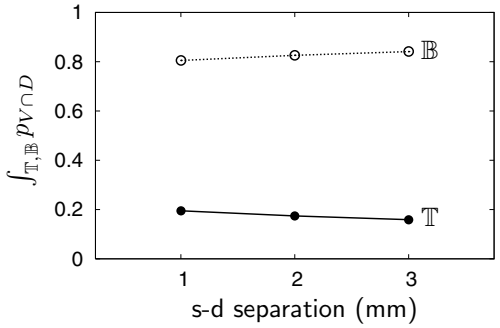

FIG. 5.2. *Interrogation density function* (5.1) *integrated over the top* $\mathbb{T}$ *and bottom* $\mathbb{B}$ *layers as a function of s-d separation.*

we mean that the light both has visited the region and is subsequently detected. This is not surprising, as the detected photons using probes with larger s-d separations will possess longer trajectories that will typically penetrate deeper into the tissue. Consistent with this bottom layer analysis, the top layer probabilities decrease by nearly 20% (from 0.195 to 0.159) as the s-d separation increases from 1 to 3 mm, indicating that the smaller s-d separations provide a considerable improvement in the interrogation of the top layer. This information drawn from our transport model assists in the design of probes for the accurate recovery of optical properties in each layer.

We next solve the inverse problem using similar probe configurations to verify the expected correlation between information given by our $P(V \cap D)$ maps and the ability of specific probe designs to determine optical property changes in one of the layers.

5.2. Perturbed tissue inverse problem. Here we discuss the impact of the interrogation maps on the accurate recovery of optical properties. To utilize information gained from our $P(V \cap D)$ maps, which are generated for various s-d separations, probes with similar features are employed for the recovery of optical properties. However, for the purpose of performing a two-parameter inverse solution, at least two detectors are required. To perform the inversion, we choose to employ six detectors to make the inverse solution more robust with respect to signal noise in the measured reflectance signal. These detectors are 200 μm in diameter and are positioned adjacent to each other to form a linear detector array that spans 1.2 mm. We solve the inverse problem with this detector array immediately adjacent to the source, resulting in s-d separations that span [0–1.2] mm. We also consider the quality of the inverse problem results in seven other configurations by moving the detector array progressively away from the source in increments of 0.2 mm. This provides measurements with eight distinct ranges of s-d separations: [0–1.2] mm, [0.2–1.4] mm, [0.4–1.6] mm, [0.6–1.8] mm, [0.8–2.0] mm, [1.0–2.2] mm, [1.2–2.4] mm, and [1.4–2.6] mm. These configurations of six detectors with a single source provide a spatially resolved measurement of reflected light. Clearly, the progressive movement of the detector array away from the source results in the interrogation of deeper layers, as already seen in Figure 5.2.

We examine two test cases that represent transformations in each layer typical of optical properties changes occurring from the development of precancer: (a) an increase in optical absorption within the lower layer due to the recruitment of increased blood flow and (b) an increase in optical scattering within the upper layer

due to local cellular transformations. Simulated spatially resolved reflectance data are generated using two-region Monte Carlo simulations with 2% Gaussian noise added. Our method to determine μ_a and μ_s uses starting values taken from our background (homogeneous) case. Perturbation and differential Monte Carlo methods [9, 10, 18] are used in a two-parameter optimization algorithm to determine the changes to these optical properties, $\hat{\mu}_a = \mu_a + \delta\mu_a$ and $\hat{\mu}_s = \mu_s + \delta\mu_s$, prescribed in one of the layers that best fit the simulated measured data. The solution identifies the layer optical properties that best match the measured data in the least squares sense. Details of the inverse solution method are described elsewhere [9, 10, 18].

5.2.1. Bottom layer μ_a perturbation. In our first test case we consider a 200% increase to μ_a relative to the background optical properties in the bottom layer. All other optical properties are held fixed. This results in the following set of optical properties: $\mu_s = 6.11/\text{mm}$, $\mu_a = 0.034$ in the top layer and $\hat{\mu}_s = 6.11/\text{mm}$, $\hat{\mu}_a = 0.068/\text{mm}$ in the bottom layer. Our two-parameter inverse solution seeks to identify and decouple both $\hat{\mu}_s$ and $\hat{\mu}_a$ successfully.

Figure 5.3 displays the recovered optical properties in the bottom layer as a function of the separation between the source and the linear array of detectors. Error bars representing one standard deviation confidence intervals are shown. The solid and dashed horizontal lines represent the true $\hat{\mu}_s$ and $\hat{\mu}_a$ values in the bottom layer, respectively. The $\hat{\mu}_s$ recovery for all ranges of s-d separation is excellent. The quality of the $\hat{\mu}_a$ estimates improves as the s-d separation increases, as is evidenced by more accurate mean values and smaller confidence intervals. This is consistent with the improved interrogation of the bottom layer at larger s-d separations as predicted by Figure 5.2.

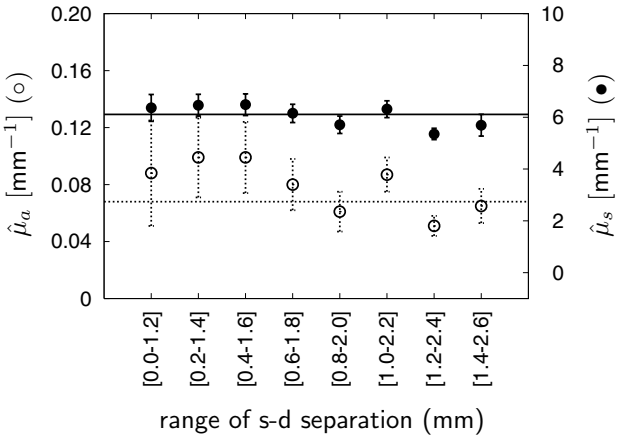

FIG. 5.3. *Recovered bottom layer absorption* (○) *and scattering* (●) *coefficients due to a* 200% μ_a *perturbation in the bottom layer as a function of the range of s-d separations provided by the detector array.*

While the inverse solution results are consistent with the features shown in Figures 5.1 and 5.2, it must be noted that these interrogation maps were generated from the background, not the perturbed system. To focus on changes in the interrogation provided by the perturbed system, we examine a map that displays the relative difference in the interrogation of the perturbed tissue as compared to the background problem (shown in Figure 5.1). Figure 5.4 provides this result, specifically a map of

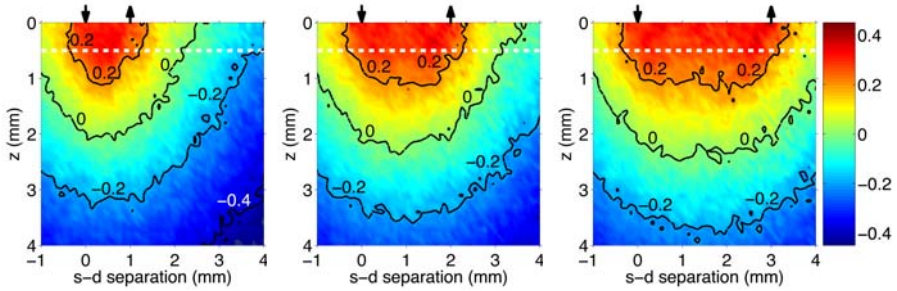

FIG. 5.4. *Plots of the relative difference between the interrogation density function for a* 200% μ_a *perturbation in the bottom layer and the background system for s-d separations of* 1, 2, *and* 3 *mm (left to right).*

$[(\hat{p}_{V\cap D} - p_{V\cap D})/p_{V\cap D}]$ for s-d separations of 1, 2, and 3 mm.

These maps display regions in which the relative difference between the interrogation of the perturbed and background medium is zero (green (0 contour)), increasingly negative (deeper blues (-0.2, -0.4 contours)), and increasingly positive (yellow-orange-red (0.2, 0.4 contours)). Negative values indicate diminished interrogation in the perturbed medium relative to the background system, while positive values indicate enhanced interrogation.

From these maps we observe that the enhancement of interrogation penetrates deeper into the bottom layer with increasing s-d separation. This is consistent with the improved inverse solution results at larger s-d separation. However, this interrogation at larger s-d separation is offset by the increased absorption in the bottom layer of the perturbed system, which depletes the detected signal. This may explain why the $\hat{\mu}_s$ predictions do not improve markedly.

To understand the contributions from each layer, we integrate the data in Figure 5.4 over the top and bottom layers, $(\int_{\mathbb{T}} \hat{p}_{V\cap D} - \int_{\mathbb{T}} p_{V\cap D})/\int_{\mathbb{T}} p_{V\cap D}$ and $(\int_{\mathbb{B}} \hat{p}_{V\cap D} - \int_{\mathbb{B}} p_{V\cap D})/\int_{\mathbb{B}} p_{V\cap D}$, respectively. From these results (shown in Figure 5.5) we see that the probability of interrogating the bottom layer is degraded slightly in the perturbed medium due to the increased absorption in that layer. Despite the detrimental effect of the increased bottom layer absorption, interrogation of the bottom layer still improves with increases of the s-d separation. This again is consistent with the inverse results shown in Figure 5.3. Figure 5.5 also displays the integrated top layer results. Although these results are not pertinent to the bottom layer inverse problem considered here, they may shed light on other inverse problems in which determination of top layer optical properties is desired within a system that is simultaneously undergoing a change in the bottom layer absorption. All top layer values are positive, indicating improved interrogation in this layer of the perturbed medium compared to the background medium due to the increased absorption in the bottom layer.

5.2.2. Top layer μ_s perturbation. We now examine a second test case involving a 120% increase in μ_s in the top layer relative to the background value. All other optical properties in both layers are held fixed. This results in the following set of optical properties: $\hat{\mu}_s = 7.332/\text{mm}$, $\hat{\mu}_a = 0.034/\text{mm}$ in the top layer and $\mu_s = 6.11/\text{mm}$, $\mu_a = 0.034/\text{mm}$ in the bottom layer. Figure 5.6 displays the recovered optical properties in the top layer as a function of the separation between the source and the linear array of detectors. The results show improved estimates in the mean values of $\hat{\mu}_s$ as well as smaller confidence intervals when the linear detector array is closer to

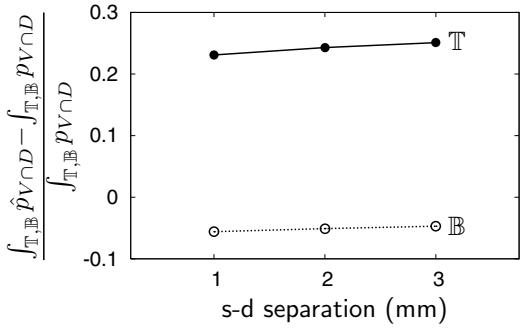

FIG. 5.5. *Relative difference between the interrogation density function for a* 200% μ_a *perturbation in the bottom layer versus the background, integrated over the top* $\mathbb{T}$ *and bottom* $\mathbb{B}$ *layers as a function of s-d separation.*

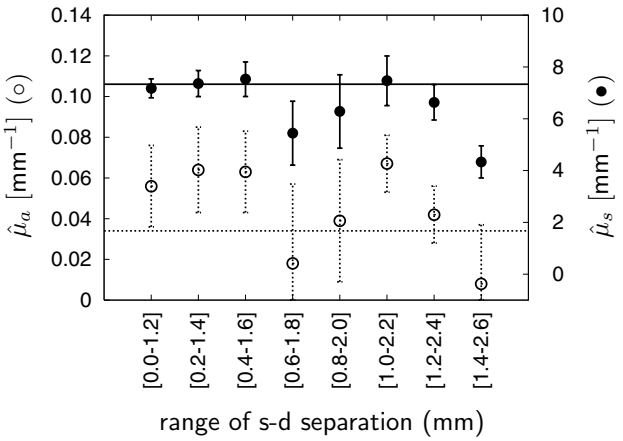

FIG. 5.6. *Recovered top layer absorption* (○) *and scattering* (●) *coefficients due to a* 120% μ_s *perturbation in the top layer as a function of the range of s-d separations provided by the detector array.*

the source. This is in line with the results shown in Figure 5.2 that showed improved interrogation of the top layer at the smaller s-d separations. The recovered mean values of $\hat{\mu}_a$ display no correlation with s-d separation.

For this case it is also useful to examine plots of the relative difference between the perturbed and background medium which are shown in Figure 5.7. The increased scattering in the top layer of the perturbed medium results in enhanced interrogation of this layer. This is especially true when the s-d separation is small, as evidenced by the deep red colors (0.2 contour) in the top layer. However, this enhancement dissipates rapidly as the s-d separation increases and indicates that the increased scattering in the top layer plays a diminishing role in the detected signal. This is easily discerned by focusing attention on the top layer and noticing that while this area is primarily red (0.2 contour) at small s-d separations, it rapidly changes to orange, yellow, and green (0.1 and 0 contours) at larger separations. Moreover, for even larger separations (not shown), this region changes to blue (-0.2 contour). This illustrates that as the s-d separation increases, the increased scattering in the top layer no longer provides an enhanced interrogation of the top layer. This occurs because the photon pathlengths between source and detector increase for larger s-d separations,

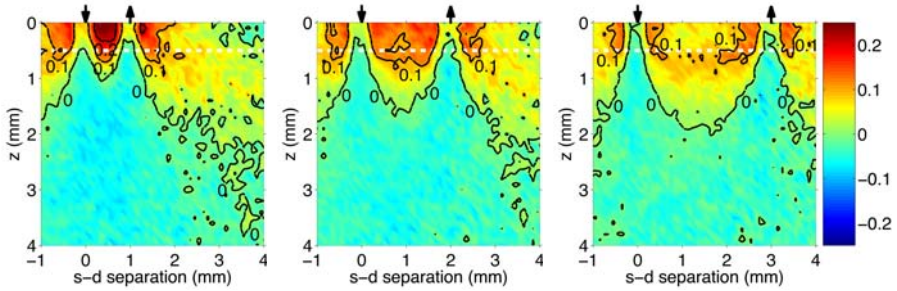

FIG. 5.7. *Plots of the relative difference between the interrogation density function for a* 120% μ_s *perturbation in the top layer and the background system for s-d separations of* 1, 2, *and* 3 *mm (left to right).*

resulting in the depletion of the detected signal by absorption in the top layer. This is the principal cause for the lack of significant improvement in the $\hat{\mu}_a$ predictions with increasing s-d separation shown in Figure 5.6.

The relative difference maps integrated over each layer are shown in Figure 5.8. These plots confirm that the integrated sampling of the top layer is enhanced in the perturbed medium but that this enhancement decreases rapidly with increasing s-d separation. Again, while the integrated bottom layer results are not directly relevant to our top layer inversion, it is interesting to observe that the increased scattering in the top layer has a diminishing effect on the bottom layer interrogation as the s-d separation increases.

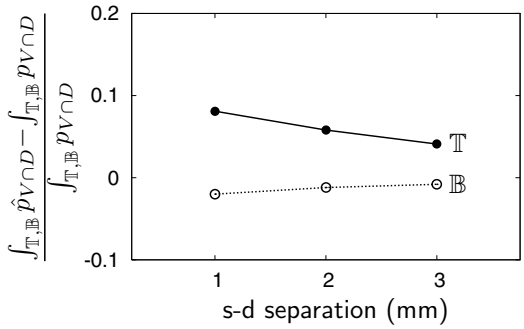

FIG. 5.8. *Relative difference between the interrogation density function for a* 120% μ_s *perturbation in the top layer versus the background, integrated over the top* $\mathbb{T}$ *and bottom* $\mathbb{B}$ *layers as a function of s-d separation.*

It is important to note that for a given medium, the $P(V \cap D)$ maps (Figures 5.1, 5.4, and 5.7) for *all* s-d separations were created from a *single* forward and a *single* adjoint Monte Carlo simulation. To achieve this degree of computational efficiency, we have made use of the symmetry of the layered problem and the probe configuration. This enables the application of linear superposition to align the two simulations for *any* selected s-d separation for the generation of the resulting $P(V \cap D)$ maps. While the use of the coupled forward-adjoint Monte Carlo technique is already more efficient than conventional Monte Carlo simulation, use of symmetry further enhances the computational efficiency of our methodology. A study of the comparative efficiency of conventional Monte Carlo simulation and the coupled forward-adjoint technique developed here is beyond the scope of this paper.

6. Summary and conclusions. We have developed a transport-based technique that determines the joint probability that photons will visit any tissue subvolume and subsequently be detected. Calculation of this conditional system response (system interrogation) is based on an extension of classical reciprocity theory for radiative transport that couples the responses of forward and adjoint Monte Carlo simulations at the boundary of any designated tissue subvolume. These maps of conditional response provide insight as to how s-d configurations affect the spatial distribution of tissue interrogation. While our maps that display the conditional system response were integrated over all angles, it is important to reiterate that angle-specific $P(V \cap D)$ maps can also be generated easily and will be of interest for many applications.

We then applied this computational methodology using data descriptive of a two-layer epithelial/stromal tissue and produced $P(V \cap D)$ maps for varying s-d separations. Moreover, we provided evidence that the maps produced by our coupled forward-adjoint Monte Carlo method provide useful and reliable guidelines for the choice of preferred probe designs, as measured by the successful recovery of optical properties from selected tissue regions.

In biomedical optics applications, the tissue volume targeted for further examination is typically large compared to both the source and detector. In these cases, the coupled forward-adjoint Monte Carlo approach will be especially advantageous from a computational efficiency standpoint. Use of variance reduction methods applied to both forward and adjoint simulations will further increase the efficiency of this new computational method.

REFERENCES

[1] R. Aronson, *Radiative transfer implies a modified reciprocity relation*, J. Opt. Soc. Amer. A, 14 (1997), pp. 486–490.

[2] F. Bevilacqua, J. S. You, C. K. Hayakawa, and V. Venugopalan, *Sampling tissue volumes using frequency-domain photon migration*, Phys. Rev. E (3), 69 (2004), 051908.

[3] D. A. Boas, M. A. O'Leary, B. Chance, and A. G. Yodh, *Detection and characterization of optical inhomogeneities with diffuse photon density waves: A signal-to-noise analysis*, Appl. Opt., 36 (1997), pp. 75–92.

[4] K. M. Case and P. F. Zweifel, *Linear Transport Theory*, Addison–Wesley, Reading, MA, 1967.

[5] S. N. Cramer, *Forward-adjoint Monte Carlo coupling with no statistical error propagation*, Nucl. Sci. Eng., 124 (1996), pp. 398–416.

[6] J. P. Culver, V. Ntziachristos, M. J. Holboke, and A. G. Yodh, *Optimization of optode arrangements for diffuse optical tomography: A singular-value analysis*, Opt. Lett., 46 (2001), pp. 701–703.

[7] S. Feng, F. Zeng, and B. Chance, *Photon migration in the presence of a single defect: A perturbation analysis*, Appl. Opt., 34 (1995), pp. 3826–3837.

[8] E. E. Graves, J. P. Culver, J. Ripoll, R. Weissleder, and V. Ntziachristos, *Singular-value analysis and optimization of experimental parameters in fluorescence molecular tomography*, J. Opt. Soc. Amer. A, 21 (2004), pp. 231–241.

[9] C. K. Hayakawa and J. Spanier, *Perturbation Monte Carlo methods for the solution of inverse problems*, in Monte Carlo and Quasi-Monte Carlo Methods 2002, Springer, Berlin, 2004, pp. 227–241.

[10] C. K. Hayakawa, J. Spanier, F. Bevilacqua, A. K. Dunn, J. S. You, B. J. Tromberg, and V. Venugopalan, *Perturbation Monte Carlo methods to solve inverse photon migration problems in heterogeneous tissues*, Opt. Lett., 26 (2001), pp. 1335–1337.

[11] L. G. Henyey and J. L. Greenstein, *Diffuse radiation in the galaxy*, Astrophys. J., 93 (1941), pp. 70–83.

[12] P. Hoel, S. Port, and C. Stone, *Introduction to Probability Theory*, Houghton Mifflin, Boston, 1971.

[13] R. Hornung, T. H. Pham, K. A. Keefe, M. W. Berns, Y. Tadir, and B. J. Tromberg, *Quantitative near-infrared spectroscopy of cervical dysplasia in vivo*, Human Reproduction,

14 (1999), pp. 2908–2916.

[14] T. Papaioannou, N. W. Preyer, Q. Fang, A. Brightwell, M. Carnohan, G. Cottone, R. Ross, L. R. Jones, and L. Marcu, *Effect of fiber-optic probe design and probe-to-target distance on diffuse reflectance measurements of turbid media: An experimental and computational study at* 337 *nm*, Appl. Opt., 43 (2004), pp. 2846–2860.

[15] M. S. Patterson, S. Andersson-Engels, B. C. Wilson, and E. K. Osei, *Absorption spectroscopy in tissue-simulating materials: A theoretical and experimental study of photon paths*, Appl. Opt., 34 (1995), pp. 22–30.

[16] T. J. Pfefer, L. S. Matchette, A. M. Ross, and M. N. Ediger, *Selective detection of fluorophore layers in turbid media: The role of fiber-optic probe design*, Opt. Lett., 28 (2003), pp. 120–122.

[17] J. C. Schotland, J. C. Haselgrove, and J. S. Leigh, *Photon hitting density*, Appl. Opt., 32 (1993), pp. 448–453.

[18] I. Seo, J. S. You, C. K. Hayakawa, and V. Venugopalan, *Perturbation and differential Monte Carlo methods for measurement of optical properties in a layered epithelial tissue model*, J. Biomed. Opt., 12 (2007), 014030.

[19] I. V. Serov, T. M. John, and J. E. Hoogenboom, *A new effective Monte Carlo midway coupling method in MCNP applied to a well logging problem*, Appl. Radiat. Isot., 49 (1998), pp. 1737–1744.

[20] I. V. Serov, T. M. John, and J. E. Hoogenboom, *A midway forward-adjoint coupling method for neutron and photon Monte Carlo transport*, Nucl. Sci. Eng., 133 (1999), pp. 55–72.

[21] M. C. Skala, G. M. Palmer, C. Zhu, Q. Liu, K. M. Vrotsos, C. L. Marshek-Stone, A. Genfron-Fitzpatrick, and N. Ramanujam, *Investigation of fiber-optic probe designs for optical spectroscopic diagnosis of epithelial pre-cancers*, Lasers Surg. Med., 34 (2004), pp. 25–38.

[22] K. Sokolov, L. T. Nieman, A. Myakov, and A. Gillenwater, *Polarized reflectance spectroscopy for pre-cancer detection*, Technology in Cancer Research and Treatment, 3 (2004), pp. 1–14.

[23] J. Spanier and E. Gelbard, *Monte Carlo Principles and Neutron Transport Problems*, Addison–Wesley, Reading, MA, 1969.

[24] T. Ueki and J. E. Hoogenboom, *Exact Monte Carlo perturbation analysis by forward-adjoint coupling in radiation transport calculations*, J. Comput. Phys., 171 (2001), pp. 509–533.

[25] T. Ueki, J. E. Hoogenboom, and J. L. Kloosterman, *Analysis of correlated coupling of Monte Carlo forward and adjoint histories*, Nucl. Sci. Eng., 137 (2001), pp. 117–145.

[26] L. Wang, S. L. Jacques, and L. Zheng, *Mcml-Monte Carlo modeling of light transport in multi-layered tissues*, Comput. Methods Programs Biomed., 47 (1995), pp. 131–146.

[27] G. H. Weiss, R. Nossal, and R. F. Bonner, *Statistics of penetration depth of photons re-emitted from irradiated tissue*, J. Mod. Opt., 36 (1989), pp. 349–359.

[28] A. J. Welch and M. van Gemert, *Optical-Thermal Response of Laser-Irradiated Tissue*, Plenum Press, New York, 1995.

[29] M. L. Williams, *Generalized contributon response theory*, Nucl. Sci. Eng., 108 (1991), pp. 355–383.

[30] M. L. Williams and W. W. Engle, *The concept of spatial channel theory applied to reactor shielding analysis*, Nucl. Sci. Eng., 62 (1977), pp. 92–104.

[31] C. Zhu, Q. Liu, and N. Ramanujam, *Effect of fiber optic probe geometry on depth-resolved fluorescence measurements from epithelial tissues: A Monte Carlo simulation*, J. Biomed. Opt., 8 (2003), pp. 237–247.